Magnetotransport properties and Fermi surface topology of the nodal line semimetal InBi

Sambhab Dan,[1] Kuldeep Kargeti,[2] R. C. Sahoo,[3] Shovan Dan,[4] Debarati Pal,[1] Sunil Verma,[1] Sujay Chakravarty,[5] S. K. Panda,[2] and S. Patil[1,*]

[1]*Department of Physics, Indian Institute of Technology (BHU), Varanasi 221005, India*
[2]*Department of Physics, Bennett University, Greater Noida 201310, Uttar Pradesh, India*
[3]*Department of Chemical Science and Engineering, Tokyo Institute of Technology, 2-12-1 Ookayama, Meguro, Tokyo 152-8552, Japan*
[4]*Department of Condensed Matter Physics and Materials Science, Tata Institute of Fundamental Research, Homi Bhabha Road, Colaba, Mumbai 400005, India*
[5]*UGC-DAE Consortium for Scientific Research, Kalpakkam Node, Kokilamedu 603104, India*

(Received 21 November 2022; accepted 17 April 2023; published 5 May 2023)

In the present study, we have thoroughly characterized the 3D Fermi surface of a topological nodal line semimetal InBi via the Shubnikov–de Haas oscillations and density functional theory. The nitty-gritty of its full 3D Fermi surface has been discussed in detail. The Fermi surface topology and the Hall conductivity emphasized the carrier compensation as a driving force for the observed extremely high magnetoresistance. The magnetotransport revealed a unique magnetic-field-induced metal-semiconducting transition. The origin of such a phenomenon has been elaborated theoretically which has implications for layered topological nodal line semimetals with linearly dispersing bands.

DOI: 10.1103/PhysRevB.107.205111

I. INTRODUCTION

The exotic band structure of topological materials has become an exciting field of inquiry nowadays due to the variety of electronic structures across different members of the family. For example, in the case of a topological insulator, there exists a symmetry-protected non-trivial surface electronic structure [1] whereas in the case of Dirac semimetals, Weyl semimetals, etc., we have, on the contrary, symmetry protected non-trivial bulk electronic structure [2]. These semimetals also possess nodal points which are the touching points of their valence and conduction bands in the momentum space. The nodal structures (i.e., the loci of nodal points in momentum space) of different topological materials discovered so far are quite rich with some newly discovered compounds within the family showing more complex structures. Thus, we have either a nodal line [3], nodal chain [4], nodal knot [5], nodal link [6–8], or nodal net [9,10], denoting the richness of the underlying phenomena among them.

A few of the recently discovered promising nodal line materials are ZrSiX (X = S, Se, Te) [11,12], Ag_2S [13], AX_2 (A = Ca, Sr, Ba; X = Si, Ge, Sn) [14], Ca_3P_2 [15], CaP_3 [16], CaTe [17], CaAuAs [18], CaAgX (X = P, As) [19], IrF_4 [4], Mg_3Bi_2 [20], XB_2 (X = Ti, Zr) [21], $SrAs_3$ [22], Co_2TiX (X = Si, Ge, or Sn) [23], Ta_3X (X = Al, Ga, Sn, Pb) [24], X_2Y (X = Ca, Sr, Ba; Y = As, Sb, Bi) [25], $YCoC_2$ [26], MnN [27], and YH_3 [28]. As the number of electronic states at the nodes in a nodal line system is more than that for a nodal point system, these compounds display various novel properties like a large spin Hall effect [29], long-range Coulomb interaction [30], and flat Landau level [31]. Quite interestingly, the effect of spin-orbit coupling on its electronic structure is such that either the nodal line remains protected by some symmetry of the system, such as inversion symmetry, reflection symmetry, or nonsymmorphic symmetry, or the nodal line gets destroyed by virtue of a gap formation resulting from the lack of such a protection [3,9,32–34]. For instance, the reflection symmetry of the Ta atomic plane protects the nodal line in $XTaSe_2$ (X = Pb, Tl) [35,36]. In the case of Cu_3PdN, nodal lines are protected by the inversion symmetry [10]. For ZrSiS [11] and InBi [37] the nodal lines are protected by nonsymmorphic symmetry. Although a vast amount of study has already been done on ZrSiS, InBi remains the least studied compound till date. InBi has two distinct nodal lines protected by nonsymmorphic symmetry [37] and it also has a topologically nontrivial type-II Dirac cone protected by fourfold cyclic symmetry [37]. The compound InBi exhibits unique transport properties, viz., extremely high magnetoresistance (XMR) [38], highly anisotropic MR [38], and pressure-induced superconductivity [39]. The compound also shows an upturn in the resistivity (ρ) [38] upon application of a magnetic field (**B**), but a detailed discussion on that topic has not been available till date. The quantum oscillation study of this compound has also been reported earlier [40], but a deep understanding of its Fermi surface topology and its role in the transport phenomena is still lacking.

In this article, we report the structural, transport, electronic band structure, and Fermi surface topology of InBi. The article is organized in the following way. We discuss the structural properties of InBi in Sec. III A. In Sec. III B, we discuss its magnetotransport properties. In this section, we elaborate on an interesting result, viz., the upturn nature in $\rho(T)$. A detailed mathematical treatment is put forward to explain the observed temperature dependency of the resistivity. Another aspect of our study is establishing the role of electron and hole carriers

*spatil.phy@iitbhu.ac.in

in the transport phenomena. Our results further unravel the origin of XMR in InBi. In Sec. III C, we discuss the Fermi surface topology by Shubnikov–de Haas (SdH) oscillations and compare it with the computed Fermi surface using density functional theory (DFT). Our DFT result satisfactorily matches the experimental data. Accumulating the empirical and theoretical tools, we have successfully mapped the compound's Fermi surface. Such an inquiry gives a complete 3D visualization of its Fermi surface. We provide a detailed discussion for each Fermi surface sheet (FS). The modulation of each FS due to the electron and hole doping and the FS's role in the transport phenomena are also discussed rigorously. At the end, we have discussed some important physical parameters derived from our SdH oscillation study.

II. EXPERIMENTAL DETAILS AND THEORETICAL METHODS

We prepared a single crystal of InBi using the modified Bridgman method. Elemental In (Alfa Aesar) and Te (Alfa Aesar), with 99.9% purity, have been used as the starting materials. The stoichiometric amounts of starting materials were taken in an evacuated (10^{-6} mbar) quartz ampoule. The ingots were then melted at 200 °C in the quartz ampoule and kept for 24 hr at that temperature. The molten ingots were subsequently cooled to 150 °C with a cooling rate of 20° hr^{-1}. Thereafter we cooled the molten material from 150 °C to 30 °C at a slow cooling rate of 3° hr^{-1}. As the bottom of the quartz tube is of a conical shape, the nucleation process starts from the bottommost point of the quartz tube. Shiny conical-shaped single crystals are thus obtained from the quartz tube. Small parts of the crystal have been used for further characterization.

X-ray diffraction (XRD) of a powdered compound was performed for the structural analysis. Further, we also performed XRD on the compound's cleaved surface to check its single crystallinity. The XRD results from the cleaved surfaces identifies various crystallographic planes with respect to their Miller indices. Only reflections from planes of certain Miller indices and their multiples were observed thus certifying the single crystallinity of the surface. The Hall study of the compound was performed on a rectangle-shaped sample with the four-point probe method in the van der Pauw configuration using a 9 T physical property measurement system (PPMS) and the Hall voltages were detected along the direction perpendicular to the current flow in the sample plane. The resistivity and the MR measurement was performed in the four-probe puck in a 15 T cryogen free magnet system (CFMS-15) from M/S Cryogenic, Ltd., UK. During MR and Hall measurements, the external magnetic field was applied perpendicular to the *ab* plane.

In order to interpret our experimental results, we have carried out density functional theory calculations using the full potential linearized augmented plane-wave based method implemented in the WIEN2k code [41]. All the calculations were performed in a non-spin-polarized setup with a generalized gradient approximation (GGA) [42] approach for the exchange-correlation functional. The spin-orbit coupling is included using a second-variational scheme and thus all the reported results are from GGA+SOC calculations. In order to obtain a very accurate Fermi energy (E_F), the $R_{mt}K_{max}$ value is considered to be 7 and Brillouin zone (BZ) integration is done using the tetrahedron method [43] with a sufficiently dense k mesh ($14\times14\times14$).

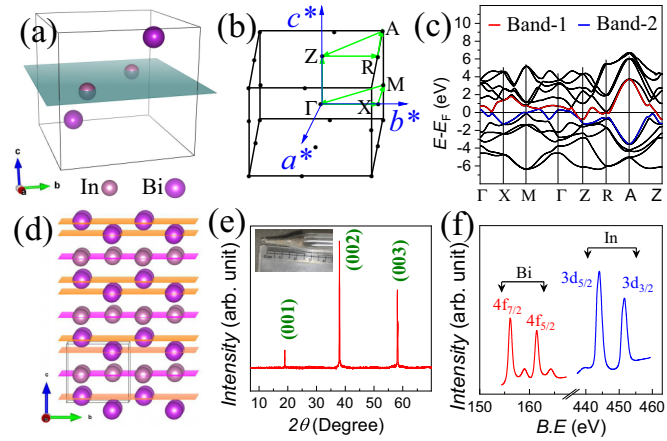

FIG. 1. (a) The unit cell of InBi compound. (b) The BZ structure and the high-symmetry points along which DFT calculation is performed. (c) The band structure along high-symmetry points. Band 1 (red) and band 2 (blue) are the only two bands that provide carriers' density at E_F. (d) The *ab* planes of InBi. (e) The XRD peaks which originated from the *ab* plane. Inset: The photograph of conical-shaped InBi single crystal. (f) The XPS spectrum of InBi.

III. RESULTS AND DISCUSSION

A. Structural characterization

We performed powder XRD in order to obtain the crystal structure of the compound. Our study suggests that the compound crystallizes in the $p4/nmm$ (space group No. 129) crystal structure. The refinement of the powder XRD pattern yields $a = 5.01(2)$ Å, $b = 5.012(2)$ Å, and $c = 4.77(9)$ Å; a unit cell containing the In and Bi atoms is shown in Fig. 1(a). The plane containing In atoms is depicted by a shaded color. The BZ with its high-symmetry points and the corresponding electronic band structure are shown in Figs. 1(b) and 1(c). The band structure indicates that only two bands crossed the E_F. We label these two bands as band 1 and band 2 which are highlighted in red and blue in Fig. 1(c), respectively. The crystal structure of this compound is layered as shown in Fig. 1(d) with the shaded planes indicating the occupancy of In and Bi atoms along the *ab* planes. Figure 1(e) shows the XRD pattern taking from the *ab* plane of the crystal. As the diffraction occurred only from the *ab* planes, the diffractogram only contains $(00l)$ peaks. The very sharp peaks of the XRD pattern indicate the good crystallinity of the compound. The $(00l)$ peak pattern is also consistent with the space group and unit cell parameters derived from the powder XRD. We show the photograph of our conical-shaped single crystal along with a centimeter scale in the inset of Fig. 1(e). The x-ray photoelectron spectroscopy (XPS) of InBi is shown Fig. 1(f). The spectrum from $4f$ and $3d$ orbitals of Bi and In atoms well verified the compound's elemental composition. The XPS spectrum also agrees with the stoichiometry of the chemical composition.

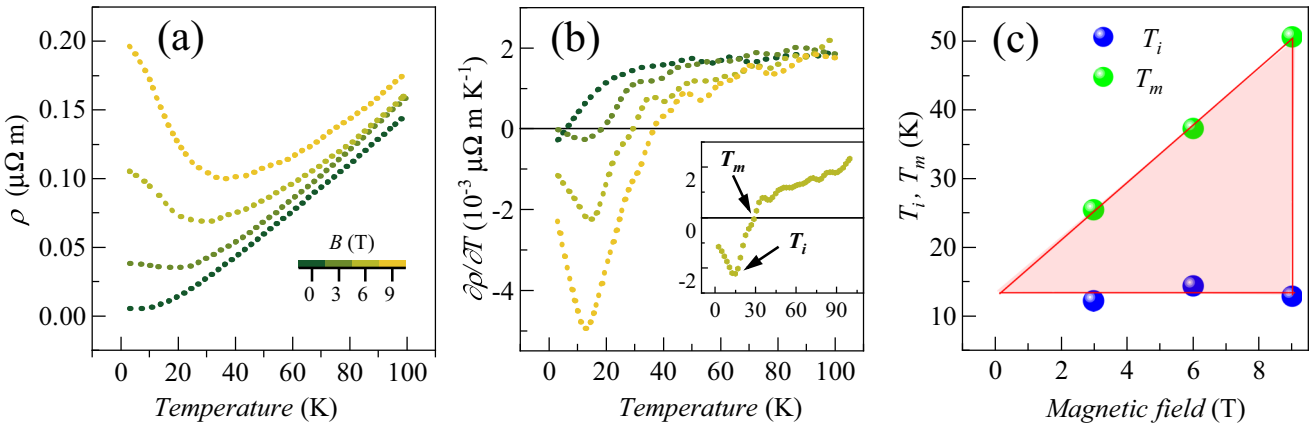

FIG. 2. (a) $\rho(T)$ measured at 3–100 K with the application of 0–9 T magnetic field. (b) After performing $\frac{\partial\rho(T)}{\partial T}$ (to calculate turn-on temperature). The T_m and T_i are indicated in the inset figure. (c) The variation of T_m and T_i with the magnetic field. Triangle formed by T_m and T_i are shown by a pink-shaded area.

B. Magnetotransport properties

1. Magnetic-field-dependent ρ(T)

The temperature-dependent resistivity measured at 3–100 K is shown in Fig. 2(a). The resistivity of the compound at 3 K and 100 K is 0.5×10^{-2} and 14.7×10^{-2} μΩ m, respectively, which is very close to the earlier reported result [38]. To calculate the residual-resistance ratio (RRR) of our compound, we performed our resistivity study up to 300 K. The RRR of the compound based on the 3 and 300 K resistivity data is estimated to be 93. The RRR of the compound in the earlier reported data lies between 91–271 [38]. We have observed that the resistivity of the compound sharply increases with the increase of magnetic field, especially in the low-temperature regime. When $\mathbf{B} = 0$, the resistivity of the compound has been increased monotonically with temperature. On applying the high magnetic field, the $\rho(T)$ rapidly decreases first, and then it increases with the increase of temperature. Such kind of upturn behavior is also observed in other nontrivial topological systems [44–48], where, applying a certain magnetic field, the $\rho(T)$ shows minima at a particular temperature (T_m).

We have shown the first-order derivative $\frac{\partial[\rho(T)]}{\partial T}$ in Fig. 2(b). The turn-on temperature is indicated in the figure as T_m, where the slope of the $\rho(T)$ changes its sign from negative to positive. Apart from turn-on behavior, we have also identified the minima of the $\frac{\partial[\rho(T)]}{\partial T}$, indicated as T_i in Fig. 2(b). The T_i of the compound is approximately estimated as 12 K, and it changes negligibly with the change of applied magnetic field. We have plotted the variation of T_m and T_i with the applied magnetic field in Fig. 2(c). The triangle formed by the T_m and T_i is one of the vital features observed in the compensated semimetals [49]. The value of the slope inside the shaded area of the triangle is negative, whereas the upper outside region of the triangle shows the positive slope. For the case of graphite and bismuth, the triangular phase diagram can be explained by the inequality $\hbar/\tau \lesssim \hbar\omega_c \lesssim k_B T$, where τ is the electron-phonon scattering time and ω_c is the cyclotron frequency [50]. In clean semimetals with low carrier density, $\tau^{-1} \ll k_B T/\hbar$, and hence, there exists a wide temperature-field range where XMR and turn-on-like behavior in resistivity appear. On the other hand, large carrier density and strong impurity scattering limit the MR in conventional metals.

We have calculated the T-dependent MR from the $\rho(T)$ data. The MR of the compound is defined as

$$\mathrm{MR} = [\rho(B,T) - \rho(0,T)]/\rho(0,T). \tag{1}$$

Here, $\rho(B,T)$ denotes the resistivity of the compound as a function of magnetic field (B) and temperature (T). The compound's MR% at 3–100 K is shown in Fig. 3(a). The MR% of the compound is very high at low temperatures. It goes up to 2500% at 9 T. We have observed that the MR% of the compound reduces drastically from 0 to 20 K and it almost becomes negligible above 40 K.

In order to analyze the temperature dependence of $\rho(0,T)$, we have fitted $\rho(0,T)$ with several functions [Fig. 3(b)]. First, in order to analyze the low-temperature region, we have fitted $\rho(0,T)$ as $A + BT^n$ (where A and B are the constants) up to 20 K. The result from the best-fitted parameter gives $n = 3$. In the second step, we fixed $n = 2$, and fitted the $\rho(0,T)$ up to 20 K. However, the fitted data using $n = 2$ are not well matched compared to the previous case. Lastly, we have fitted $\rho(0,T)$ in the whole temperature range, and the best-fitted parameter for that scenario gives $n = 1.44$. In the last case, the fitted data are well matched in high temperature, but they do not fit well in the low-temperature region. The observation of $n = 3$ for our case indicates the departure of pure electron dominated scattering. Generally, $n = 2$ is observed for pure electron-correlated dominated scattering [51]. Similar kinds of behaviors ($n = 3$) are also observed for other compensated semimetals, viz., LaSbTe [52] and LaBi [53]. Semimetal LaSb ($n = 4$) [46], elemental yttrium [54], and transition-metal carbide [55] also show interband electron-phonon scattering.

2. Origin of turn-on behavior

The MR of the compound based on Kohler's law [56,57] is defined as

$$\mathrm{MR} = \alpha[B/\rho(0,T)]^m. \tag{2}$$

Comparing Eqs. (1) and (2), we get

$$\rho(B,T) = \{\alpha B^m/[\rho(0,T)]^{m-1}\} + \rho(0,T). \tag{3}$$

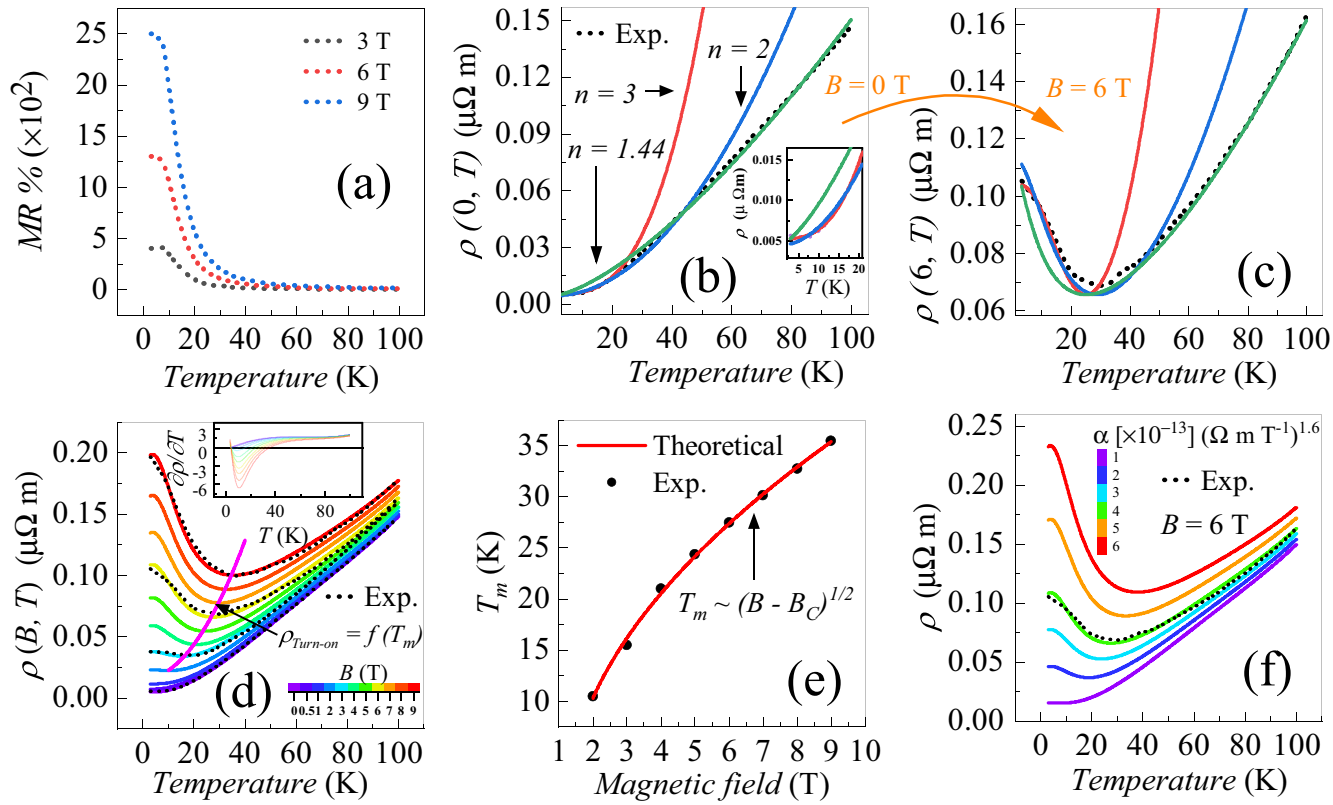

FIG. 3. (a) Calculated MR% with the application of 3 T, 6 T, and 9 T magnetic field. (b) Experimental $\rho(T)$ without any magnetic field and different type of fitted functions. Data up to 20 K are shown in the inset figure. (c) Experimental and simulated $\rho(T)$ with the application of the 6 T magnetic field. The color code for the different n remains the same as previously. (d) Simulated $\rho(T)$ under the application of 0–9 T magnetic field. Experimental $\rho(T)$ (shown as black dashed lines) is plotted over the theoretically generated one. The $\rho_{\text{turn-on}}$ as a function of T_m is indicated by a solid magenta line. The $\frac{\partial\rho(T)}{\partial T}$ of the theoretically generated patterns are shown in the inset figure. (e) Variation of turn-on temperature as a function of B and the fitted pattern. (f) Simulated $\rho(6, T)$ with the variation of α.

Using Eq. (3), we have simulated the $\rho(T)$ under the 6 T magnetic field. During the simulation, we have fixed $\alpha = 1.2\times10^{-13}$ $(\Omega\,\text{m}\,\text{T}^{-1})^{1.6}$ and $m = 1.6$, which are derived from the Kohler's law fitting [Eq. (2)]. Ideally, $m = 2$ for the perfectly compensated system, but our result $m = 1.6$ suggests that our compound slightly departs from the perfectly compensated case. The simulated patterns of $\rho(6, T)$ along with the experimental data are shown in Fig. 3(c). Our study suggests that simulated $\rho(6, T)$, derived from the experimental $\rho(0, T)$, reasonably matches the experimental $\rho(6, T)$. We have also predicted $\rho(6, T)$ for all the corresponding cases of $\rho(0, T)$. Our simulated $\rho(6, T)$ in Fig. 3(c) follows the same color code for the corresponding cases of $\rho(0, T)$ in Fig. 3(b). The result suggests that for $n = 3$ and 2, the theoretically generated $\rho(6, T)$ matches well at low temperature but deviates at high temperature. For the case of $n = 1.44$, the simulated $\rho(6, T)$ fairly matches the experimental one at high temperature.

Using Eq. (3), we have simulated $\rho(B, T)$ for 0.5–9 T. We have plotted the theoretically generated $\rho(B, T)$ in Fig. 3(d). The result matches the experimental data excellently. The experimental data are plotted as a black dashed line over the corresponding simulated pattern. Such an analysis validates our theoretical approach that replicates the experimental $\rho(B, T)$. We have also shown the first-order derivative of $\rho(B, T)$ in the inset of Fig. 3(d) in order to calculate the turn-on temperature (T_m). The derived T_m and the corresponding magnetic field are plotted in Fig. 3(e). The variation of turn-on temperature with respect to the magnetic field is fitted with the equation

$$T_m = \zeta(B - B_c)^{\nu}. \tag{4}$$

Such a formula was initially proposed by Khveshchenko [58] and is validated for graphene and bismuth. For graphite and bismuth, $\nu = 1/2$. The best-fitted parameters in our case give $\zeta = 12.75$ K $\text{T}^{-0.5}$, $B_c = 1.36$ T, and $\nu = 1/2$. $\nu = 1/2$ suggests that the turn-on nature of our compound follows the aforementioned picture.

The above theory suggests that the magnetic field opens an excitonic gap (in pyrolitic graphite) in the linear spectrum of the Coulomb interacting quasiparticles, and hence the compound shows semiconducting-like transport features. Further studies suggest that such kind of band gap opening is not just limited to a particular compound; rather it is observed across a wide range of compounds [46,52]. One can calculate the semiconducting gap (Δ) by $\log(\rho)$ vs T^{-1} fitting as $\rho(T) \propto \exp(\Delta/K_BT)$ within $T_i < T < T_m$ [46,52]. Such a phenomena of a Coulomb-interaction driven electronic instability is found to occur in a layered system possessing linear band dispersion at E_F under applied magnetic field [58]. Since our system

too is layered and possesses linear band dispersions close to E_F, an excitonic gap could open up there, following the same phenomena. The excitonic gap for our compound at 3 T, 6 T, and 9 T is 0.098 meV, 0.612 meV, and 0.869 meV, respectively (see the Supplemental Material [59]). However, a saturation is observed in the resistivity at low temperatures which is ubiquitous in semiconductors [61] and other 2D metals [62,63]. In our case too we have observed the saturation below T_i which does not also show any dependence on the excitonic gap or the applied magnetic field. It rather originates from those bands which are not gapped thus providing charge carriers for the conduction. These carriers are liable to get scattered by the impurities at low temperatures thus giving rise to the saturation.

In Fig. 3(f), we simulate $\rho(B, T)$ with the variation of α. In the simulation, we fixed $B = 6$ T, and observe how the variation of α affects the turn-on behavior. Our analysis suggests that the lower the α the higher the critical magnetic field needed to produce turn-on behavior. The analysis indicates that if $\alpha < 0.48\times10^{-13}$ $(\Omega\,\mathrm{m\,T^{-1}})^{1.6}$, we could not observe any turn-on behavior even at 6 T. The analysis highlights a significant role of α in the turn-on phenomena.

In this section, we provide a mathematical analysis for the turn-on behavior. We define a resistivity minima at T_m as $\rho_{\text{turn-on}}$. To calculate the minima in $\rho(B, T)$, we take $\frac{\partial[\rho(T,B)]}{\partial T}$ and make it zero at $T = T_m$. The mathematics is followed as

$$\frac{\partial[\rho(B, T)]}{\partial T}_{T=T_m} = 0. \tag{5}$$

Solving Eq. (5), we get

$$\rho(0, T_m) = \alpha^{1/m}(m-1)^{1/m}B. \tag{6}$$

To calculate the resistivity at turn-on temperature, we put $T = T_m$ in Eq. (3). The equation follows as

$$\rho(B, T_m) = \alpha^{1/m}(m-1)^{1/m}\left(\frac{1}{m-1}+1\right)B. \tag{7}$$

From Eq. (4), we already know that the parameter T_m is a explicit function of B. Hence, putting the value of B from Eq. (4) to Eq. (7), we get $\rho_{\text{turn-on}}$ as a function of T_m. After rewriting Eq. (7), we get

$$\rho_{\text{turn-on}}(T_m) = \alpha^{1/m}(m-1)^{1/m}\left(\frac{1}{m-1}+1\right)\left(\frac{T_m^2}{\zeta^2}+B_c\right). \tag{8}$$

Equation (8) is valid for a particular compound that shows a similar kind of upturn nature in $\rho(T)$ on the application of magnetic field. Putting the value of $\alpha = 1.2\times10^{-13}$ $(\Omega\,\mathrm{m\,T^{-1}})^{1.6}$, $m = 1.6$, $\zeta = 12.75$ K $\mathrm{T}^{-0.5}$, and $B_c = 1.36$ T, Eq. (8) in our case becomes

$$\rho_{\text{turn-on}}(T_m) = \left(\frac{T_m^2}{163}+1.36\right)\times10^{-8}. \tag{9}$$

We plot Eq. (9) in Fig. 3(d). The magenta line in the figure indicates the $\rho_{\text{turn-on}}$. The simulated $\rho_{\text{turn-on}}$ based on Eq. (9) excellently matches with the experimental results. The details of the analytical part are written in the Appendix.

Based on the above analyses of the transport properties, we concluded the following: First, without the application of a magnetic field resistivity of the compound follows as $A+BT^n$. At low temperatures $n = 3$. But at high temperatures n becomes 1.44. Second, based on Eq. (3), we have generated a two-dimensional data set (containing B and T) that fully replicates the experimental data. We have shown the simulated resistivity and its first derivative in a 3D contour plot in Figs. 4(a) and 4(b). Third, the parameter α has a significant role in producing the turn-on behavior in $\rho(T)$. Turn-on phenomena can disappear if α becomes lower than a critical value. Finally, we can calculate the resistivity at the turn-on temperature (T_m) from our algebraic expression.

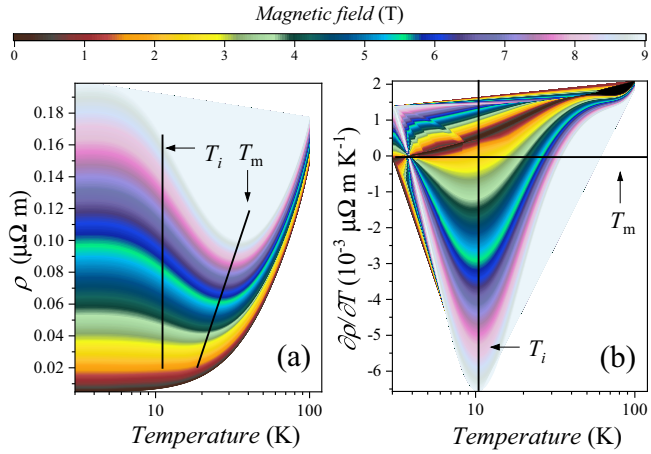

FIG. 4. 3D contour plot of simulated data. (a) $\rho(B, T)$. (b) $\frac{\partial[\rho(B,T)]}{\partial T}$.

3. *Temperature-dependent $\rho(B)$*

The variation of $\rho(B)$ at several temperatures is shown in Fig. 5(a). We have shown that the change of resistivity with temperature is very high when applied magnetic field is very low and $\rho(B)$ for all temperatures tend to converge at high magnetic fields. It is observed that with the increase of B, $\rho(B, 3)$ first grows and then it almost catches up to the value of $\rho(B, 15)$, $\rho(B, 25)$, and $\rho(B, 50)$ at 3 T, 4 T, and 6 T, respectively. The MR% as a function of B is shown in Fig. 5(b). The MR% of the compound is very high at 10 K and reaches up to 2500% at 3 K. On the other hand, MR% at high temperatures reduces drastically and almost becomes negligible above 25 K. We have also shown MR% vs $B/\rho(T, 0)$ for all the temperatures in Fig. 5(c). The log-log plot of all the data points falls in a single straight line. The fitted line based on Eq. (2) is shown by a solid magenta line. During the fitting, we have put a corresponding value of α and m as stated earlier. The fitted data at 3 K before the log-log plotting are shown in the inset of Fig. 5(c). The falling of all data points in a straight line also verified our earlier assumption that the parameters α and m are almost temperature-insensitive in our compound.

4. *Hall resistivity study*

The Hall effect study in 0–9 T magnetic field at different temperatures is shown in Fig. 6. To eliminate the MR contribution from the Hall data, we performed the Hall study in the forward and reverse bias of the magnetic fields. As the MR does not change its sign while reversing the magnetic

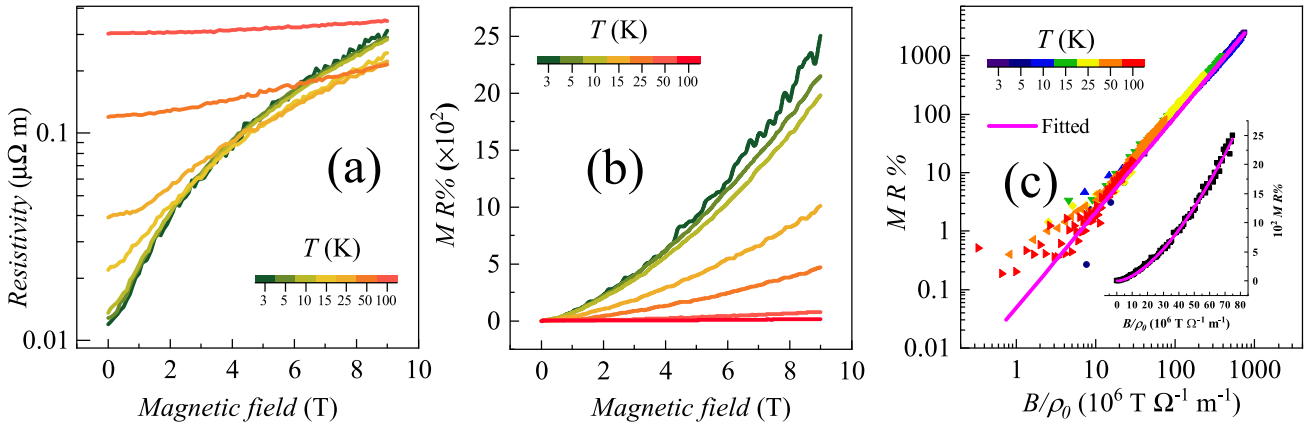

FIG. 5. (a) The $\rho(B)$ measured at 3–100 K with the application of 0–9 T magnetic field. (b) The MR% as a function of B that is calculated from the experimental $\rho(B)$. (c) The log-log plot of MR% as a function of $B/\rho(0, T)$. The fitted line based on Kohler's law is shown in a solid magenta line. The fitted line for 3 K is separately shown in the inset figure.

field unlike Hall resistivity, we subtract these two (data for forward and reverse bias) Hall data from each other and then divide them by two to get the actual Hall contribution. We followed the same process at 3 K, 10 K, 25 K, and 50 K in the full range of the magnetic fields. The nonlinear behavior of the Hall resistivity suggests that both the carriers (electron and hole) contribute to the transport phenomena. The raw Hall data contained noise. The Hall data which are shown in the figure are plotted after smoothing the raw data (for more details, see the Supplemental Material [59]). The whole set of the Hall data that are shown in Fig. 6 is reproducible, as we repeat the measurement using different pieces of a single crystal along with the current variations. We have observed that at $T < 25$ K, $\rho_{xy}(B)$ increases rapidly. On the application

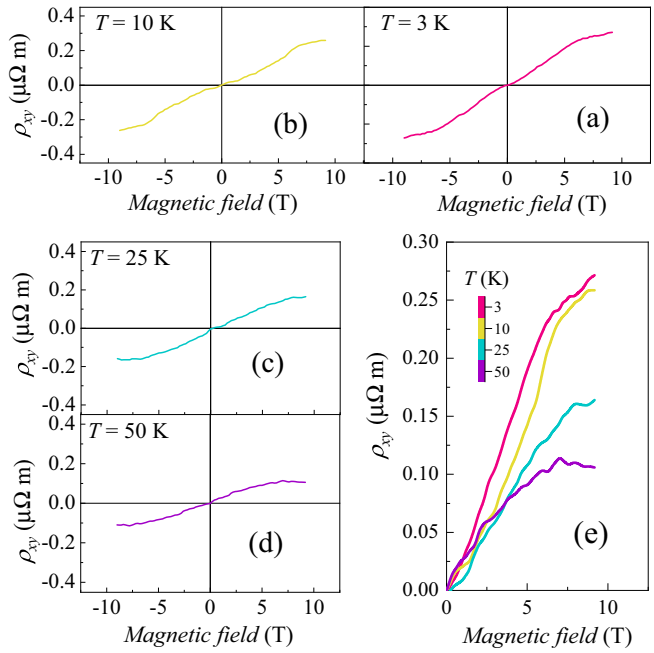

FIG. 6. The $\rho_{xy}(B)$ from +9 T to −9 T at (a) 3 K, (b) 10 K, (c) 25 K, and (d) 50 K. (e) The $\rho_{xy}(B)$ from 0–9 T with the temperature range 3–50 K.

of 9 T magnetic field, ρ_{xy} at 3 K is almost twice compared to the ρ_{xy} at 25 K. Interestingly, the change in MR% calculated from ρ_{xx} also is twice at the same temperature and magnetic field.

Using the experimental result of $\rho_{xx}(B)$ and $\rho_{xy}(B)$, we have calculated the $\sigma_{xx}(B)$ and $\sigma_{xy}(B)$. After the inverting of the resistivity matrix, $\sigma_{xx}(B)$ and $\sigma_{xy}(B)$ can be written as

$$\sigma_{xx}(B) = \frac{\rho_{xx}(B)}{[\rho_{xx}(B)]^2 + [\rho_{xy}(B)]^2}, \tag{10}$$

$$\sigma_{xy}(B) = \frac{\rho_{xy}(B)}{[\rho_{xx}(B)]^2 + [\rho_{xy}(B)]^2}. \tag{11}$$

Based on Eqs. (10) and (11), the calculated $\sigma_{xx}(B)$ and $\sigma_{xy}(B)$ are plotted in Figs. 7(a) and 7(b).

We have fitted $\sigma_{xx}(B)$ and $\sigma_{xy}(B)$ with a two-band, two-carrier model [64] stated as

$$\sigma_{xx}(B) = e\left[n_h\mu_h\frac{1}{1+(\mu_h B)^2} + n_e\mu_e\frac{1}{1+(\mu_e B)^2}\right], \tag{12}$$

$$\sigma_{xy}(B) = eB\left[n_h\mu_h^2\frac{1}{1+(\mu_h B)^2} - n_e\mu_e^2\frac{1}{1+(\mu_e B)^2}\right]. \tag{13}$$

As stated both the carrier types contribute to our transport phenomena; we have performed the global fitting based on the two-carrier model where the simultaneous presence of the electron and hole carrier is considered. Here the electron density (n_e), the hole density (n_h), the electron mobility (μ_e), and the hole mobility (μ_h) are termed as fitting parameters. The fitted lines are shown as a solid red line in Figs. 7(a) and 7(b). Extracted parameters from Eqs. (12) and (13) give almost the same result. The fitting parameters, viz., $n_e(T)$, $n_h(T)$, $\mu_e(T)$, and $\mu_h(T)$, are shown in Figs. 7(c) and 7(d).

From Fig. 7(c), it is observed that $n_e(T)$ is slightly higher at 3 K but, as a broad view the $n_e(T)$ and $n_h(T)$ are approximately the same ($\sim 1.5\times10^{-26}$ m^{-3}) below 25 K. After 25 K, $n_e(T)$ almost remains the same and $n_h(T)$ increases to $\sim 7\times10^{-26}$ m^{-3}. The results suggest that the number of electrons and holes contribute equally at lower temperatures whereas, at high temperatures, the transport is dominated by holes. Observing the MR data from Fig. 5(b), we observed that MR% is also very large below 25 K. Such kind of corre-

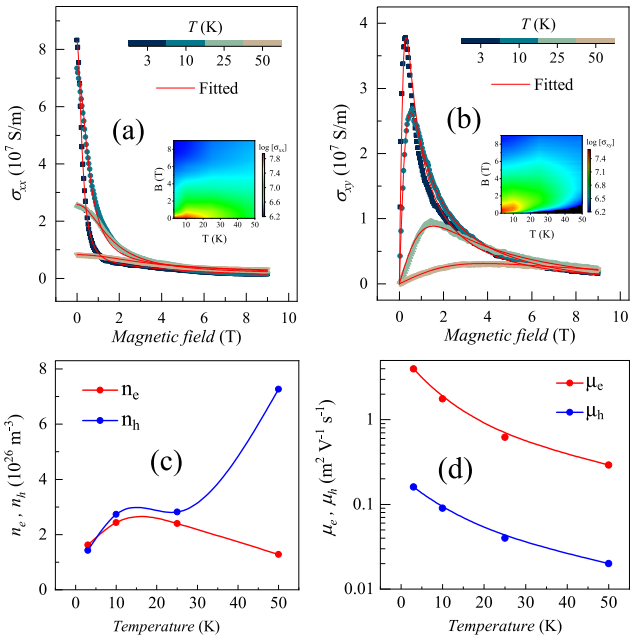

FIG. 7. (a) $\sigma_{xx}(B)$ and its corresponding fittings; inset: logarithmic plot of $\sigma_{xx}(B)$ as a function of magnetic field and temperature in a 3D contour plot. (b) $\sigma_{xy}(B)$ and its corresponding fittings; inset: logarithmic plot of $\sigma_{xy}(B)$ as a function of magnetic field and temperature in a 3D contour plot. (c) The temperature-dependent electron and hole density which are estimated from the two-carrier model. (d) The temperature-dependent electron and hole mobility which are estimated from the two-carrier model.

lation hints that the XMR is accompanied by the electron-hole compensation of the compound. Regarding the carrier mobility, we have observed that the electron mobility of the compound at 3 and 15 K is 3.98 and 0.29 $m^2\,V^{-1}\,s^{-1}$, respectively. The hole mobility at 3 K and 15 K is 25 and 15 times lower than the corresponding electron mobility at those temperatures. The effective mobility ($\mu_{\text{eff}} \sim \sqrt{\mu_e \mu_h}$) at 3 K is 0.79 $m^2\,V^{-1}\,s^{-1}$ which is consistent with the previous report [38].

C. Shubnikov–de Haas oscillation and Fermi surface topology study

1. *The FS topology of* InBi

Before introducing the experimental part, we have discussed the basic electronic structure of InBi. Our study suggests that only two bands contribute to the carrier's density at E_F. The energy dispersion of band 1 and band 2 is shown in Fig. 8 where the allowed electron- and hole-like states are shown in the red and blue shaded areas, respectively. Figure 8 indicates that γ and α pockets coming from band 1 are electron types. Similarly, β and δ pockets coming from band 2 are hole types. We have shown the 3D Fermi surface in Fig. 9. The FS coming out from band 1 creates two distinct pockets γ and α placing at high-symmetric points Z and R, respectively. Similarly, the FS coming out from band 2 creates two distinct pockets β and δ placing at high-symmetric points Γ and M, respectively.

After identifying all the electron and hole pockets, we have calculated the extremum area of these pockets. To draw the extrema, we take several cuts in the k_x-k_y plane in the 3D BZ. The contours from several cuts perpendicular to the k_z axis are shown in Fig. 10. The red and blue contours come from band 1 and band 2, respectively. Figures 10(b)–10(e) suggest that the extremum area of β and δ sheets lies at the Γ point. The cut corresponding to the Γ point is shown in Fig. 10(b) where maxima of the FS are indicated by an arrow. It is visible that the area of the β and δ sheets continuously decreases from cut 1 to cut 4. Similarly, from cut 5 to cut 8, the area of the γ and α sheets continuously increases. The maximum area of the γ and α sheets lies at the Z point (cut 8). The extremum area of the γ and α sheets is indicated by the arrow in Fig. 10(i). The extremum area of all four FSs is listed in Table I.

2. *Experimental verification*

The quantum oscillation work of InBi was performed by Saito [65] in 1964. In this same work, the author performed de Haas–van Alphen (dHvA) oscillation for InBi. After Saito's work, many authors performed the quantum oscillation study, but none of them successfully resolved the nature of electron

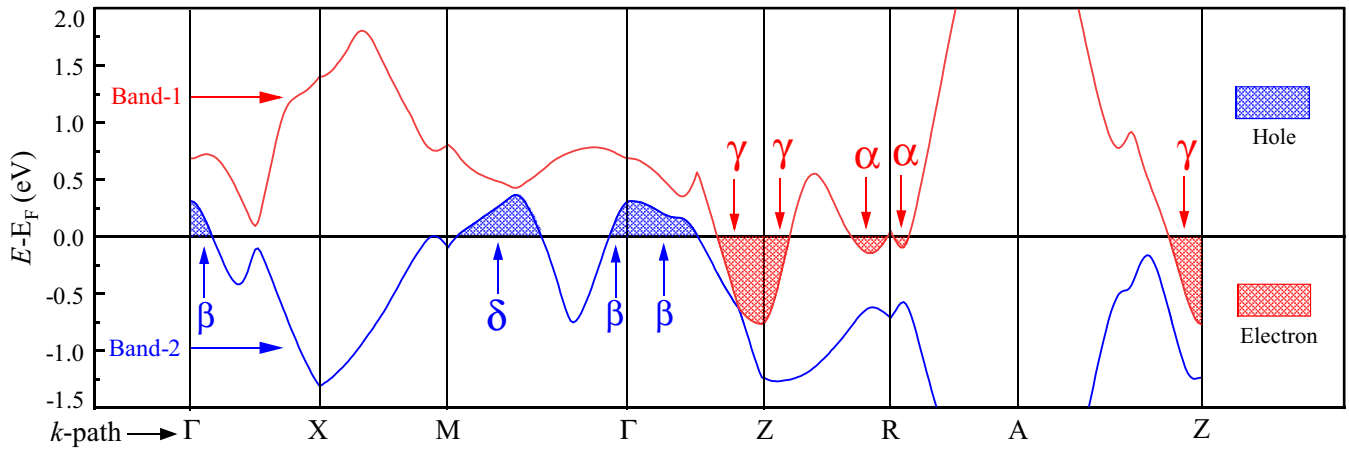

FIG. 8. The band structure of band 1 is shown in red. The allowed states marked by red-shaded area denote the electron-like pocket. The γ and α pockets are generated from band 1. The band structure of band 2 is shown in blue. The allowed states marked by blue-shaded area denote the hole-like pockets. The β and δ pockets are generated from band 2.

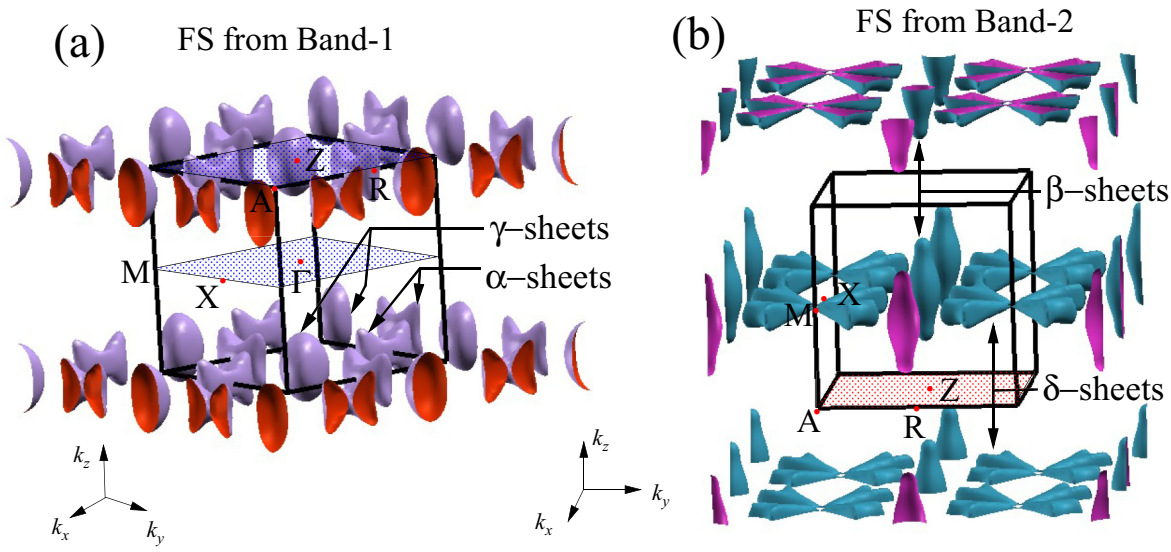

FIG. 9. (a) The electron pockets come from band 1. The γ and α sheets are lying at high-symmetric Z and R points respectively. (b) The hole pockets come from band 2. The β and δ sheets are lying at high-symmetric Γ and M points, respectively.

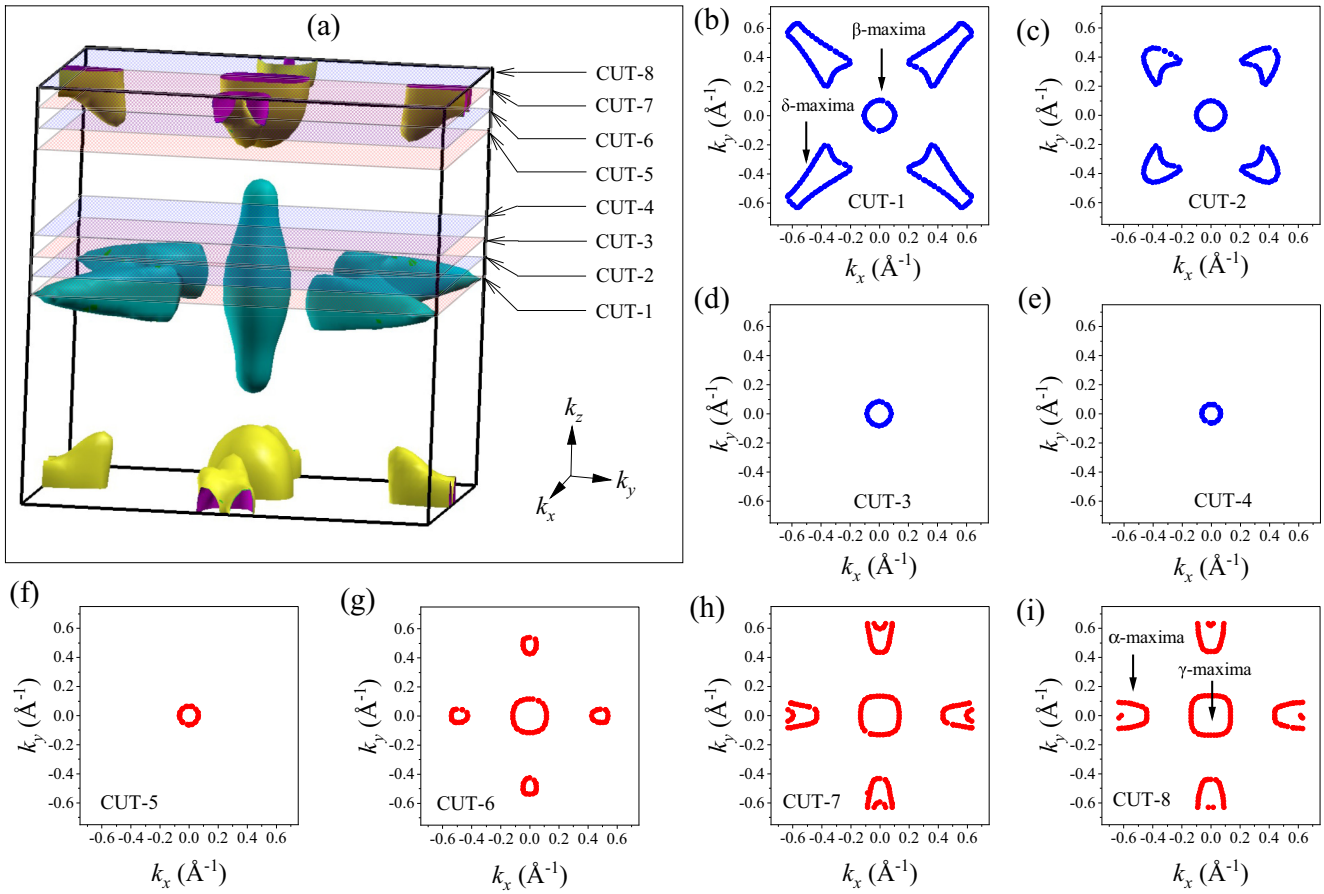

FIG. 10. Fermi sheets in k_x-k_y plane at several k_z cuts. (a) Several k_x-k_y planes in 3D BZ where the 2D contours are plotted. (b)–(d) The contours in blue coming from band 2. The areas of β and δ sheets are continuously decreasing from cut 1 to cut 4. The arrow mark in cut 1 indicates the extremum area of the corresponding pockets. (f)–(i) The contours in red coming from band 1. The areas of α and γ sheets are continuously increasing from cut 5 to cut 8. The arrow mark in cut 8 indicates the extremum area of the corresponding pockets.

TABLE I. Fermi sheet properties.

FS pocket	Origin	Type	Experimental SdH[a] frequency (T)	Experimental area[b] (nm^{-2})	Theoretical area[c] (nm^{-2})
β	Band 2	Hole	330	3.1	3.4
δ	Band 2	Hole	543	5.1	5.3
α	Band 1	Electron	Merged with β		3.3
γ	Band 1	Electron	792	7.5	6.7

[a]At 3 K and **B** along the c axis.
[b]Area derived from our SdH frequency.
[c]Extremum area (from our DFT calculation) in k_x-k_y plane.

and hole pocket from the oscillatory data. In 1973 Meyer *et al.* [40] performed a dHvA study of InBi in all crystallographic directions. We have shown part of Meyer's result in Fig. 12 as a reference. The author predicts that F_β and F_γ are originating from the InBi and F_δ is originating from the impurity band. Observing the angular variation of dHvA oscillation, Meyer *et al.* first predicted that the 3D topology of the FS originating from F_β and F_γ should be a distorted ellipsoid. From the angle-dependent data, they cannot reveal the origin of each FS from the BZ structure. We brought Meyer's result as it plays a crucial role in the context of our current study. We started our experiment with magnetotransport studies, viz., MR at low temperature and high magnetic field. To get the SdH signal, we measured MR at 3 K, 5 K, 10 K, and 15 K in the **B** field 7–15 T. The MR data and corresponding FFT spectrum are shown in Figs. 11(b) and 11(a), respectively. To perform FFT, we first plot the resistivity as a function of the inverse magnetic field. Then we take the double derivative to subtract the background. The advantage of taking the double derivative is that it eliminates the background but retains all oscillatory components. We use this data as a timescale spectrum to perform the FFT. After identifying the frequency that comes from the Fermi surface of the compound, we take an inverse FFT for the particular frequency to visualize the timescale spectrum of the particular frequency component. The range of frequencies that are used to take the deconvolution are as follows: $F_\beta \rightarrow$ 316–341 T, $F_\delta \rightarrow$ 528–553 T, and $F_\gamma \rightarrow$ 780–804 T. The range is decided based on the width of the corresponding frequency peaks observed in the FFT spectrum [Fig. 11(a)]. A detailed discussion regarding the oscillatory data is put in the Supplemental Material [59]. All FFT peaks named as F_β, F_δ, and F_γ are highlighted in

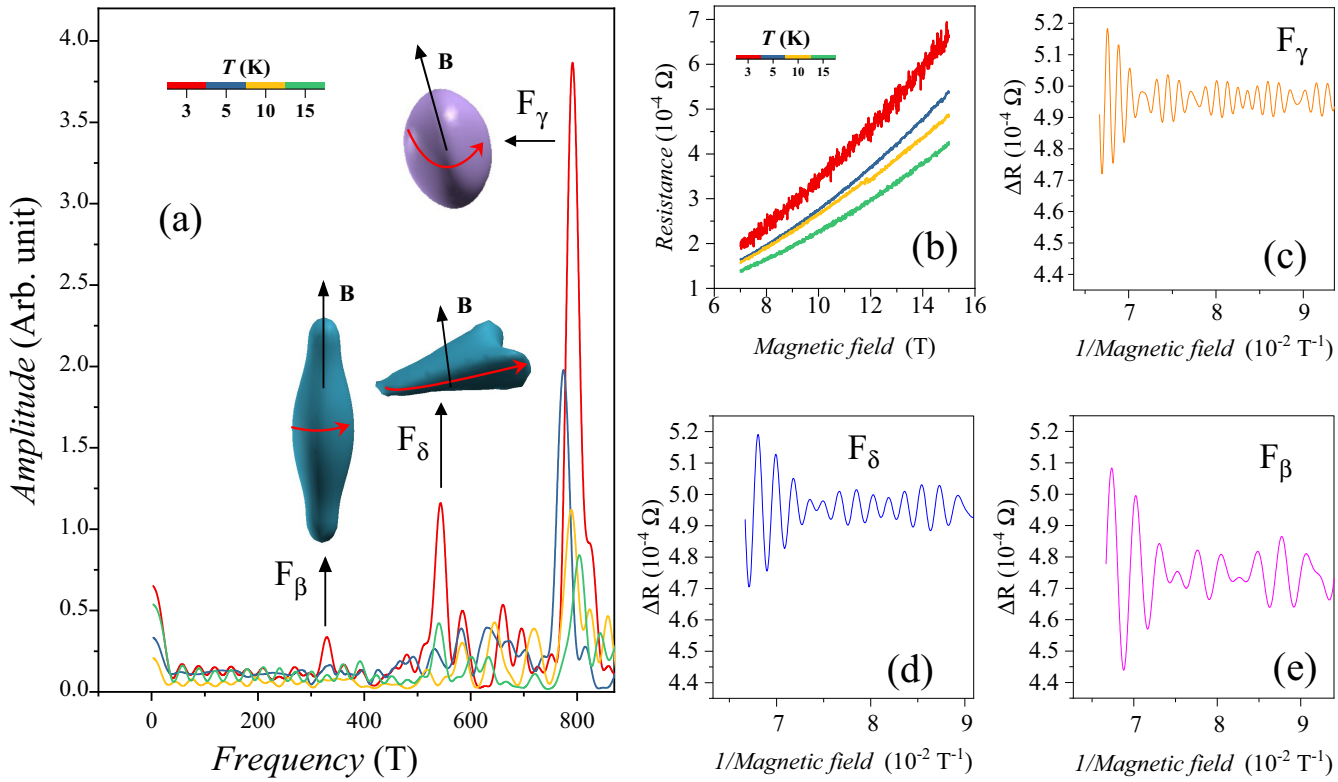

FIG. 11. The FFT spectrum and SdH oscillation. (a) The FFT spectrum calculated at 7–15 T field from the second derivative of the MR data. The red arrow indicates the extremum orbits of the corresponding pockets from where frequency peaks are coming. (b) The actual MR data from where FFT is performed. (c)–(e) The deconvoluted spectrum coming from corresponding pocket at 3 K.

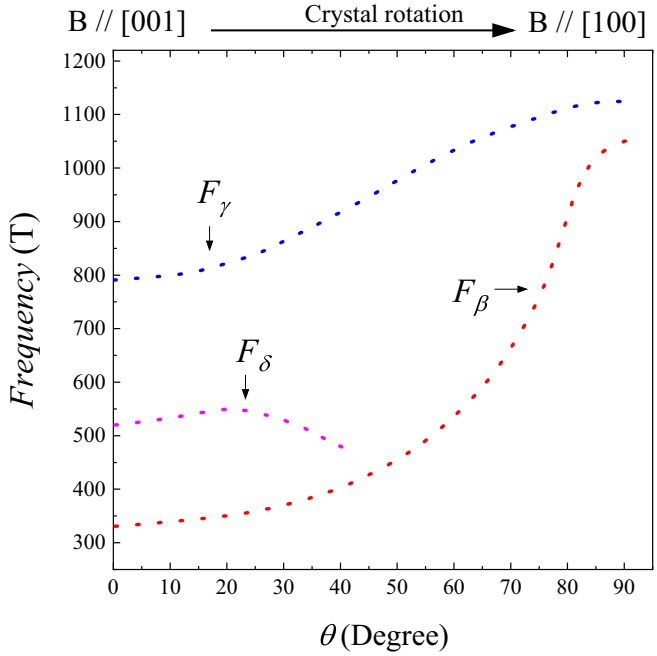

FIG. 12. Data taken from Meyer *et al.* [40]. Angle-dependent variation of three major frequencies F_β, F_γ, and F_δ.

Fig. 11(a). The timescale spectrum for the corresponding frequency peaks is shown in Figs. 11(c)–11(e). The oscillations shown in the Figs. 11(c)–11(e) are the raw oscillations derived from the 3 K MR data. We observed a considerable amount of beat formation in the timescale spectrum. The formation of beats (originating from the frequency broadening) in the oscillations is a common occurrence for any compound [66]. Regarding the FFT spectra [Fig. 11(a)] of the compound, we observed many small peaks between 550–650 T, which might come from several factors. Peaks observed at higher temperatures are in the main contributed by thermal noise which is random in nature. The small peaks (585 T and 660 T) observed at 3 K are interesting. The peak at 660 T is exactly double of F_β (330 T) which signifies that it is the harmonic of F_β. The peak at 585 T might originate from other factors, viz., inhomogeneity of the sample, nonuniformity of the source magnetic field, or spreading of crystal orientation (dislocation).

3. *Frequency from β sheets (F_β)*

The F_β of the FFT spectrum is observed at 330 T as shown in Fig. 11(a). The extremum area of the corresponding FS is close to our theoretical calculation (see Table I). As shown in Fig. 13(j), the 3D shape of the β pocket looks like a distorted ellipsoid structure. The angle-dependent study of F_β by Meyer *et al.* is shown by a red dashed line in Fig. 12. It indicates that if we change the crystal orientation from [001] to [100], F_β changes from 330 T to 1052 T. The angular dependency of F_β suggests that the semimajor axis of the pocket is 3.3 times longer than its semiminor axis. Such kind of experimental result is very consistent with our theoretically generated FS structure. Our theoretical calculation also suggests that if we move the E_F slightly upward (electron doped), the pocket size becomes lower. Our system might behave as an electron-doped compound, as it shows slightly lower FS area than the theoretical one.

4. *Frequency from δ sheets (F_δ)*

The F_δ of the FFT spectrum is observed at 543 T as shown in Fig. 11(a). The origin of the particular frequency was not established earlier. Our study suggests that the F_δ comes from the distorted triangular shape FS lying at the M point. This FS has a fourfold symmetry as shown in Figs. 13(k)–13(m). Figure 13(l) indicates that at $E = E_F$ the four petals are connected and electrons can move through the FS to make a complete loop. The extremum orbit of the electron path is marked by a red dashed line. There is an additional possibility that electrons can circulate within a single petal of the FS as the linkage between two petals is infinitesimally small. Our study suggests that any finite upward movement of E_F can disconnect the linkage among the petals. We show an example in Fig. 13(m) where a 10 meV upward shift of E_F (electron-doped) breaks the connection among petals. As our system behaves as an electron-doped one (as discussed earlier), we can easily assume that the four petals are disconnected from each other and electrons move through the extremum orbit within a single petal as shown in Fig. 13(m). The theoretically calculated extremum area of a single petal is very close to the experimental one which unambiguously supports the claim stated earlier. The DFT calculation slightly overestimates the FS area, indicating the electron-doped system.

The structure of the δ pockets at different angles is shown in Fig. 13(c). Observing the 3D nature of the pockets, we can say that the area of the pocket in the k_x-k_y plane is much larger than the area along the k_x-k_y plane. Interestingly, F_δ from angle-dependent dHvA changes according to this FS topology. The angular variation of F_δ is shown by the dashed magenta line in Fig. 12. The data suggest that when the crystal lies in [001], F_δ has its highest value. But with the tilting toward [100], F_δ started to decrease. As the area of the pocket in k_x-k_y is very small, no signal was observed along [100] direction. Such an angle-dependent study again strongly verifies the nature of the FS.

5. *Frequency from α sheets (F_α)*

The frequency corresponding to the α sheet is not observed by us because the extremum areas of the α and β sheets are very close to each other (see Table I) and hence both frequencies are superimposed to each other. We show how the FS evolves from hole doping to electron doping in Figs. 13(g)–13(i) for the completeness of our study. We observed that a 100 meV downward shift of E_F (hole doping) can break the α sheet into two equal parts. On the other hand a 100 meV upward shift of E_F (electron doping) enhances the volume of the FS. The extremum orbit in the k_x-k_y plane is indicated by the red arrow in Fig. 13(h).

6. *Frequency from γ sheets (F_γ)*

F_γ is observed at 792 T in the FFT spectrum as shown in Fig. 11(a). The FS area corresponding to γ sheets is the largest and most intense compared to all other pockets. The particular frequency comes from ellipsoid-shaped FS lying at the Z point

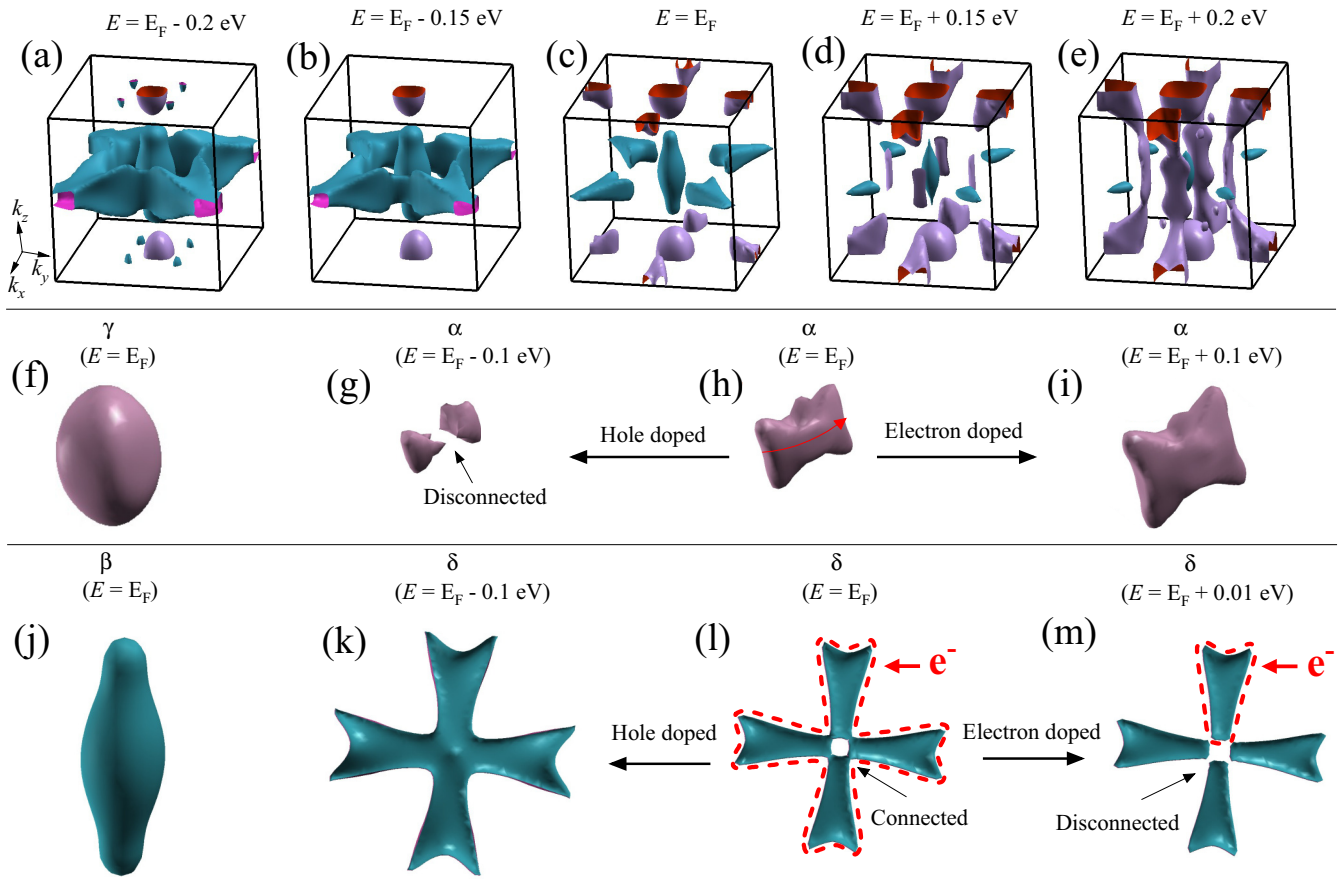

FIG. 13. The variation of FS from hole doping to electron doping. (a)–(e) The evolution of 3D BZ from hole doping to electron doping. (f) The shape of the γ pocket at $E = E_F$. (g)–(i) The evolution of α pocket from hole doped to electron doped. The extremum orbit parallel to k_x-k_y plane is shown by the red arrow. The substantial hole doping split the α pocket by two parts. (j) The shape of the β pocket at $E = E_F$. (k)–(m) The evolution of β pocket from hole doped to electron doped. The extremum orbit parallel to k_x-k_y plane is shown by red dotted line.

of the BZ. The 3D shape of the γ pocket is shown in Fig. 13(f) The angle-dependent study of F_γ is shown by the blue dashed line in Fig. 12. It indicates that if we change the crystal orientation from [001] to [100], F_γ changes from 790 T to 1124 T. The angular dependency of F_γ suggests that the semimajor axis of the pocket is 1.5 times longer than its semiminor axis. Such kind of experimental result is very consistent with our theoretically generated FS structure. Unlike the β and δ, the experimental FS area of the γ pocket is slightly lower than the theoretically predicted one (see Table I). Lowering the FS area of any electron pocket is justifiable for an electron-doped system. The amplitude of F_γ shows the adequate temperature dependency that helps us to calculate the "effective mass." The parameters, viz., "effective mass" and "Dingle temperature," derived from the F_γ are discussed in detail in the subsequent section.

D. The study of effective mass and Dingle temperature

The oscillation pattern of the resistivity is described by the Lifshitz-Kosevich (L-K) formula

$$\Delta R \propto -B^{\lambda} R_T R_D R_S \sin\left[2\pi\left(\frac{F}{B} - \Gamma - \Delta\right)\right], \qquad (14)$$

where $R_T = \alpha T\mu/B\sinh(\alpha T\mu)$, $R_D = \exp(-\alpha T_D\mu/B)$, and $R_S = \cos(\pi g\mu/2)$. μ is the ratio of the effective cyclotron mass m^* to free electron mass m_0. T_D is the Dingle temperature, and $\alpha = (2\pi^2 k_B m_0)/(\hbar e)$. The oscillation phase is described as a sine term with an additional phase factor $\Gamma - \Delta$, in which $\Gamma = \frac{1}{2} - \phi_B/2\pi$ and ϕ_B is the Berry phase. The dimensionality of FS is determined by the phase shift Δ. For 2D FS, $\Delta = 0$. For 3D FS, Δ can take the value $\pm 1/8$ according to the minima and maxima of the FS area. The Berry phase in our case is not robust and hence we do not draw any conclusive remark regarding the topics. The unreliable Berry phase can originates from the insufficient maximum field in the quantum oscillation study [46]. The term λ is also determined by the FS dimensionality. λ can take the value $\frac{1}{2}$ and 0 for 3D and 2D FS, respectively. From the L-K formula, the effective mass m^* can be calculated from the fit of the thermal damping factor R_T with the temperature dependence amplitude of the oscillation. From the SdH oscillation, we have observed that an adequate T-dependent signal comes only from F_γ. From the T-dependent amplitude damping, we have calculated the effective mass (m^*) of the electron. The fitting of R_T for the F_γ is shown in Fig. 14(a). The derived m^* from the calculation is approximately $0.40\times m_0$. Putting the value of m^*, we have theoretically estimated the Dingle temperature (T_D). The amplitude of the oscillation with

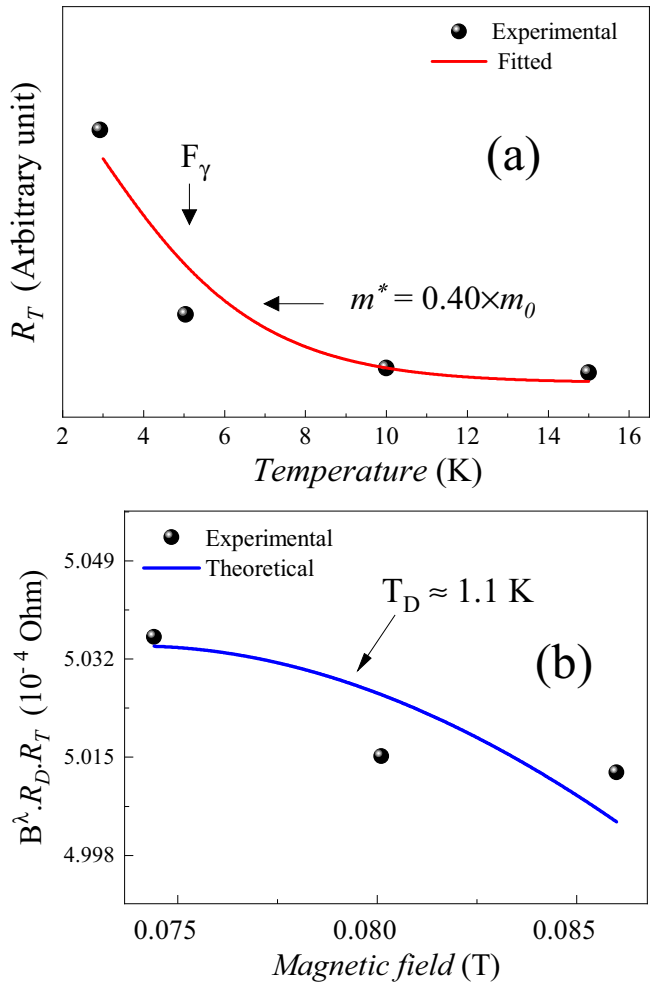

FIG. 14. (a) Calculation of m^* from T-dependent amplitude of SdH oscillation. (b) The amplitude simulation using *L-K* formula to derive T_D.

varying T_D is shown in Fig. 14(b). Our estimated T_D from the fitted data is approximately 1.1 K. The Dingle temperature of the compound has a microscopic origin closely related to the carrier's scattering. Our low T_D indicates that sample has low imperfections, viz., dislocations and mosaic structure [66].

Using the Dingle temperature T_D (∼1.1 K), we have calculated the quantum relaxation time $\tau_q = \hbar/2\pi k_B T_D = 1.20\times10^{-12}$ s and quantum mobility $\mu_q = e\tau_q/m^* = 0.53\ \mathrm{m^2\,V^{-1}\,s^{-1}}$. All estimated parameters from the F_γ are listed in Table II. The quantum mobility (μ_q) at 3 K is very close to the compound's effective mobility (μ_{eff}) estimated from Hall data at the same temperature. The consistent result suggests that our experimental outcome from SdH oscillation and the Hall measurement is very reliable. Our estimated quantum mobility is slightly lower than the classical mobility. Such a phenomenon is expected because quantum mobility is sensitive to both small-angle and large-angle scattering. On the other hand, classical Drude's mobility is only influenced by large-angle scattering [67].

TABLE II. Parameters derived from the F_γ oscillation. m^*, effective mass; T_D, Dingle temperature; τ, relaxation time; and μ_q, quantum mobility.

m^* (units of m_0)	T_D (K)	τ (ps)	μ_q ($\mathrm{m^2\,V^{-1}\,s^{-1}}$)
0.40	1.1	1.2	0.53

IV. CONCLUSION

We investigated the magnetotransport and the 3D Fermi surface of InBi. The Fermi surface topology along with the measured carrier concentrations revealed a near-perfect electron-hole compensation in the ground state, thus suggesting its relevance as a driving force for the XMR. The SdH oscillations were found to be quite rich as most of the FS contributing to the oscillations. The quantum oscillation study also helped to estimate important parameters (effective mass and Dingle temperature) of InBi. We also elaborated the origin of the observed metal-semiconductor transition by fusing the conventional Kohler's picture of MR in metals with some earlier findings. The magnetic-field-dependent T_m revealed that our system is likely to undergo a Coulomb-interaction-driven electronic instability. An excitonic band gap at the E_F was thus assumed to be opened by the application of a magnetic field in our case thus highlighting the electronic instability in the layers of the topological nodal line semimetals under the action of magnetic field.

ACKNOWLEDGMENTS

S.P. acknowledges financial support from DST-SERB, India, under Project No. ECR/2017/001243. Sambhab Dan thanks Arkadeb Pal for helping in a scientific collaboration. One of the authors, Shovan Dan, would like to thank SERB, India (Grant No. PDF/2021/004624), for financial assistance.

APPENDIX: ALGEBRAIC ANALYSIS OF THE RESISTIVITY UPTURN

The MR of the compound is defined as

$$\mathrm{MR} = [\rho(B,T) - \rho(0,T)]/\rho(0,T). \tag{A1}$$

According to Kohler's law,

$$\mathrm{MR} = \alpha[B/\rho(0,T)]^m. \tag{A2}$$

From Eq. (A1) and Eq. (A2), we get

$$\begin{aligned} \Rightarrow [\rho(B,T) - \rho(0,T)]/\rho(0,T) &= \alpha[B/\rho(0,T)]^m \\ \Rightarrow \rho(B,T) - \rho(0,T) &= \alpha B^m \rho(0,T)^{1-m}, \\ \rho(B,T) &= \alpha B^m \rho(0,T)^{1-m} \\ &\quad + \rho(0,T). \end{aligned} \tag{A3}$$

Equation (A3) expresses the resistivity as a function of magnetic field and temperature. So, if zero field $\rho(T)$ is known, one can generate a complete two-dimensional data set of resistivity from Eq. (A3) as was discussed in Sec. III B 2.

Role of α for generating resistivity minima

The right-hand side of Eq. (A3) contains two terms. The first term is a "decaying" term (for $m > 1$), whereas the second term is a "growing" term. If the value of α becomes substantially low, the "growing" term dominates and we cannot get resistivity minima. If α increases, the "decaying" term starts to dominate and we get a critical value of α at where the turn-on nature begins to show. If α increases further, the "decaying" term becomes stronger and hence the decaying nature of the resistivity follows up to higher temperature. So, the higher the α, the higher the turn-on temperature. If α increases further, the whole resistivity pattern becomes decaying and we cannot get any resistivity minima in the particular range of temperature. So the role of α is crucial as it decide whether we get turn-on-like behavior in the desired magnetic field and temperature range.

For the minima of the resistivity,

$$\begin{aligned}
&\frac{\partial[\rho(B,T)]}{\partial T}_{T=T_m} = 0\\
&\Rightarrow \frac{\partial[\rho(B,T)]}{\partial T}_{T=T_m} = \alpha B^m (1-m)[\rho(0,T_m)]^{-m}\\
&\frac{\partial[\rho(0,T_m)]}{\partial T} + \frac{\partial[\rho(0,T_m)]}{\partial T}\\
&\Rightarrow \frac{\partial[\rho(0,T_m)]}{\partial T}\{1+\alpha B^m(1-m)[\rho(0,T_m)]^{-m}\} = 0.
\end{aligned}$$

In the above equation the term $\frac{\partial[\rho(0,T_m)]}{\partial T} = \frac{\partial[\rho(0,T)]}{\partial T}_{T=T_m} \neq 0$, so the remaining term would be

$$\begin{aligned}
&\Rightarrow \{1+\alpha B^m(1-m)[\rho(0,T_m)]^{-m}\} = 0\\
&\Rightarrow \{\alpha B^m(1-m)[\rho(0,T_m)]^{-m}\} = -1\\
&\Rightarrow [\rho(0,T_m)]^m = \alpha B^m(m-1)\\
&\Rightarrow \rho(0,T_m) = \alpha^{1/m}(m-1)^{1/m}B. \qquad \text{(A4)}
\end{aligned}$$

Now, putting $T = T_m$ in Eq. (A3), we get

$$\rho(B,T_m) = \alpha B^m \rho(0,T_m)^{1-m} + \rho(0,T_m).$$

Putting the value of $\rho(B,T_m)$ [from Eq. (A4)] in the above equation, we get

$$\begin{aligned}
\Rightarrow \rho(B,T_m) &= \alpha B^m[\alpha^{1/m}(m-1)^{1/m}B]^{1-m}\\
&\quad + \alpha^{1/m}(m-1)^{1/m}B\\
\Rightarrow \rho(B,T_m) &= \alpha^{1/m}B(m-1)^{\frac{1-m}{m}} + \alpha^{1/m}B(m-1)^{1/m}\\
\Rightarrow \rho(B,T_m) &= \alpha^{1/m}\left[(m-1)^{\frac{1-m}{m}} + (m-1)^{1/m}\right]B. \qquad \text{(A5)}
\end{aligned}$$

Equation (A5) suggests that the turn-on resistivity increases linearly with the magnetic field. If the variation of turn-on temperature with respect to the magnetic field is followed as

$$T_m = \zeta(B - B_c)^{\nu}. \qquad \text{(A6)}$$

Here critical magnetic field (B_c) and other constants, viz., ζ and ν, in the equation are sample-dependent parameters. The expression of B from Eq. (A6) can be written as

$$\begin{aligned}
&\Rightarrow \left(\frac{T_m}{\zeta}\right)^{\frac{1}{\nu}} = B - B_c\\
&\Rightarrow B = B_c + \left(\frac{T_m}{\zeta}\right)^{\frac{1}{\nu}}. \qquad \text{(A7)}
\end{aligned}$$

Putting the value of B in Eq. (A5), we get

$$\Rightarrow \rho(T_m) = \alpha^{1/m}\left[(m-1)^{\frac{1-m}{m}} + (m-1)^{1/m}\right]\left[B_c + \left(\frac{T_m}{\zeta}\right)^{\frac{1}{\nu}}\right]. \qquad \text{(A8)}$$

This is a final equation which shows how turn-on resistivity varies with turn-on temperature. Equation (A8) is shown by the magenta line of Fig. 3(d).

[1] J. E. Moore, The birth of topological insulators, Nature (London) **464**, 194 (2010).

[2] N. P. Armitage, E. J. Mele, and A. Vishwanath, Weyl and Dirac semimetals in three-dimensional solids, Rev. Mod. Phys. **90**, 015001 (2018).

[3] A. A. Burkov, M. D. Hook, and L. Balents, Topological nodal semimetals, Phys. Rev. B **84**, 235126 (2011).

[4] T. Bzdušek *et al.*, Nodal-chain metals, Nature (London) **538**, 75 (2016).

[5] R. Bi, Z. Yan, L. Lu, and Z. Wang, Nodal-knot semimetals, Phys. Rev. B **96**, 201305(R) (2017).

[6] Z. Yan, R. Bi, H. Shen, L. Lu, S.-C. Zhang, and Z. Wang, Nodal-link semimetals, Phys. Rev. B **96**, 041103(R) (2017).

[7] P.-Y. Chang and C.-H. Yee, Weyl-link semimetals, Phys. Rev. B **96**, 081114(R) (2017).

[8] W. Chen, H.-Z. Lu, and J.-M. Hou, Topological semimetals with a double-helix nodal link, Phys. Rev. B **96**, 041102(R) (2017).

[9] Y. Kim, B. J. Wieder, C. L. Kane, and A. M. Rappe, Dirac Line Nodes in Inversion-Symmetric Crystals, Phys. Rev. Lett. **115**, 036806 (2015).

[10] R. Yu, H. Weng, Z. Fang, X. Dai, and X. Hu, Topological Node-Line Semimetal and Dirac Semimetal State in Antiperovskite Cu_3PdN, Phys. Rev. Lett. **115**, 036807 (2015).

[11] L. M. Schoop, M. N. Ali, C. Straßer, A. Topp, A. Varykhalov, D. Marchenko, V. Duppel, S. S. Parkin, B. V. Lotsch, and C. R. Ast, Dirac cone protected by non-symmorphic symmetry and three-dimensional Dirac line node in ZrSiS, Nat. Commun. **7**, 11696 (2016).

[12] M. M. Hosen, K. Dimitri, I. Belopolski, P. Maldonado, R. Sankar, N. Dhakal, G. Dhakal, T. Cole, P. M. Oppeneer, D. Kaczorowski, F. Chou, M. Z. Hasan, T. Durakiewicz, and M. Neupane, Tunability of the topological nodal-line semimetal phase in ZrSiX-type materials (X = S, Se, Te), Phys. Rev. B **95**, 161101(R) (2017).

[13] H. Huang, K.-H. Jin, and F. Liu, Topological nodal-line semimetal in nonsymmorphic *Cmce*-phase Ag_2S, Phys. Rev. B **96**, 115106 (2017).

[14] H. Huang, J. Liu, D. Vanderbilt, and W. Duan, Topological nodal-line semimetals in alkaline-earth stannides, germanides, and silicides, Phys. Rev. B **93**, 201114(R) (2016).

[15] Y.-H. Chan, C.-K. Chiu, M. Y. Chou, and A. P. Schnyder, Ca_3P_2 and other topological semimetals with line nodes and drumhead surface states, Phys. Rev. B **93**, 205132 (2016).

[16] Q. Xu, R. Yu, Z. Fang, X. Dai, and H. Weng, Topological nodal line semimetals in the CaP_3 family of materials, Phys. Rev. B **95**, 045136 (2017).

[17] Y. Du, F. Tang, D. Wang, L. Sheng, E.-j. Kan, C.-G. Duan, S. Y. Savrasov, and X. Wan, CaTe: A new topological node-line and Dirac semimetal, npj Quantum Mater. **2**, 3 (2017).

[18] B. Singh, S. Mardanya, C. Su, H. Lin, A. Agarwal, and A. Bansil, Spin-orbit coupling driven crossover from a starfruitlike nodal semimetal to Dirac and Weyl semimetal state in CaAuAs, Phys. Rev. B **98**, 085122 (2018).

[19] D. Takane, K. Nakayama, S. Souma, T. Wada, Y. Okamoto, K. Takenaka, Y. Yamakawa, A. Yamakage, T. Mitsuhashi, K. Horiba *et al.*, Observation of Dirac-like energy band and ring-torus Fermi surface associated with the nodal line in topological insulator CaAgAs, npj Quantum Mater. **3**, 1 (2018).

[20] T.-R. Chang, I. Pletikosic, T. Kong, G. Bian, A. Huang, J. Denlinger, S. K. Kushwaha, B. Sinkovic, H.-T. Jeng, T. Valla *et al.*, Realization of a type-II nodal-line semimetal in Mg_3Bi_2, Adv. Sci. **6**, 1800897 (2019).

[21] R. Lou, P. Guo, M. Li, Q. Wang, Z. Liu, S. Sun, C. Li, X. Wu, Z. Wang, Z. Sun *et al.*, Experimental observation of bulk nodal lines and electronic surface states in ZrB_2, npj Quantum Mater. **3**, 43 (2018).

[22] Y. K. Song, G. W. Wang, S. C. Li, W. L. Liu, X. L. Lu, Z. T. Liu, Z. J. Li, J. S. Wen, Z. P. Yin, Z. H. Liu, and D. W. Shen, Photoemission Spectroscopic Evidence for the Dirac Nodal Line in the Monoclinic Semimetal $SrAs_3$, Phys. Rev. Lett. **124**, 056402 (2020).

[23] G. Chang, S.-Y. Xu, H. Zheng, B. Singh, C.-H. Hsu, G. Bian, N. Alidoust, I. Belopolski, D. S. Sanchez, S. Zhang *et al.*, Room-temperature magnetic topological Weyl fermion and nodal line semimetal states in half-metallic Heusler Co_2TiX (X = Si, Ge, or Sn), Sci. Rep. **6**, 38839 (2016).

[24] X. Zhang, Z.-M. Yu, Z. Zhu, W. Wu, S.-S. Wang, X.-L. Sheng, and S. A. Yang, Nodal loop and nodal surface states in the Ti_3Al family of materials, Phys. Rev. B **97**, 235150 (2018).

[25] C. Niu, P. M. Buhl, G. Bihlmayer, D. Wortmann, Y. Dai, S. Blügel, and Y. Mokrousov, Two-dimensional topological nodal line semimetal in layered X_2Y (X = Ca, Sr, and Ba; Y = As, Sb, and Bi), Phys. Rev. B **95**, 235138 (2017).

[26] Y. Xu, Y. Gu, T. Zhang, C. Fang, Z. Fang, X.-L. Sheng, and H. Weng, Topological nodal lines and hybrid Weyl nodes in $YCoC_2$, APL Mater. **7**, 101109 (2019).

[27] S.-S. Wang, Z.-M. Yu, Y. Liu, Y. Jiao, S. Guan, X.-L. Sheng, and S. A. Yang, Two-dimensional nodal-loop half-metal in monolayer MnN, Phys. Rev. Mater. **3**, 084201 (2019).

[28] D. Shao, T. Chen, Q. Gu, Z. Guo, P. Lu, J. Sun, L. Sheng, and D. Xing, Nonsymmorphic symmetry protected node-line semimetal in the trigonal YH_3, Sci. Rep. **8**, 1467 (2018).

[29] Y. Sun, Y. Zhang, C.-X. Liu, C. Felser, and B. Yan, Dirac nodal lines and induced spin Hall effect in metallic rutile oxides, Phys. Rev. B **95**, 235104 (2017).

[30] Y. Huh, E.-G. Moon, and Y. B. Kim, Long-range Coulomb interaction in nodal-ring semimetals, Phys. Rev. B **93**, 035138 (2016).

[31] J.-W. Rhim and Y. B. Kim, Landau level quantization and almost flat modes in three-dimensional semimetals with nodal ring spectra, Phys. Rev. B **92**, 045126 (2015).

[32] C. Fang, Y. Chen, H.-Y. Kee, and L. Fu, Topological nodal line semimetals with and without spin-orbital coupling, Phys. Rev. B **92**, 081201(R) (2015).

[33] C. Fang, H. Weng, X. Dai, and Z. Fang, Topological nodal line semimetals, Chin. Phys. B **25**, 117106 (2016).

[34] H. Weng, Y. Liang, Q. Xu, R. Yu, Z. Fang, X. Dai, and Y. Kawazoe, Topological node-line semimetal in three-dimensional graphene networks, Phys. Rev. B **92**, 045108 (2015).

[35] G. Bian, T.-R. Chang, H. Zheng, S. Velury, S.-Y. Xu, T. Neupert, C.-K. Chiu, S.-M. Huang, D. S. Sanchez, I. Belopolski, N. Alidoust, P.-J. Chen, G. Chang, A. Bansil, H.-T. Jeng, H. Lin, and M. Z. Hasan, Drumhead surface states and topological nodal-line fermions in $TlTaSe_2$, Phys. Rev. B **93**, 121113(R) (2016).

[36] G. Bian, T.-R. Chang, R. Sankar, S.-Y. Xu, H. Zheng, T. Neupert, C.-K. Chiu, S.-M. Huang, G. Chang, I. Belopolski *et al.*, Topological nodal-line fermions in spin-orbit metal $PbTaSe_2$, Nat. Commun. **7**, 10556 (2016).

[37] S. A. Ekahana, Investigation of topological nodal semimetals through angle-resolved photoemission spectroscopy, Ph.D. thesis, University of Oxford, 2018.

[38] K. Okawa, M. Kanou, H. Namiki, and T. Sasagawa, Extremely large magnetoresistance induced by hidden three-dimensional Dirac bands in nonmagnetic semimetal InBi, Phys. Rev. Mater. **2**, 124201 (2018).

[39] V. Tissen, V. Degtyareva, M. Nefedova, E. Ponyatovskii, and W. Holzapfel, Superconductivity and crystallographic transitions of InBi under pressure, J. Phys.: Condens. Matter **10**, 7303 (1998).

[40] R. T. W. Meyer, J. Hofmans, and A. De Vroomen, The de Haas-van Alphen effect in InBi, J. Phys. Chem. Solids **35**, 307 (1974).

[41] K. Schwarz and P. Blaha, Solid state calculations using WIEN2k, Comput. Mater. Sci. **28**, 259 (2003).

[42] J. P. Perdew, K. Burke, and M. Ernzerhof, Generalized Gradient Approximation Made Simple, Phys. Rev. Lett. **77**, 3865 (1996).

[43] P. E. Blöchl, O. Jepsen, and O. K. Andersen, Improved tetrahedron method for Brillouin-zone integrations, Phys. Rev. B **49**, 16223 (1994).

[44] C. Shekhar, A. K. Nayak, Y. Sun, M. Schmidt, M. Nicklas, I. Leermakers, U. Zeitler, Y. Skourski, J. Wosnitza, Z. Liu *et al.*, Extremely large magnetoresistance and ultrahigh mobility in the topological Weyl semimetal candidate NbP, Nat. Phys. **11**, 645 (2015).

[45] J. Hu, J. Liu, D. Graf, S. Radmanesh, D. Adams, A. Chuang, Y. Wang, I. Chiorescu, J. Wei, L. Spinu *et al.*, π Berry phase and Zeeman splitting of Weyl semimetal TaP, Sci. Rep. **6**, 18674 (2016).

[46] F. Tafti, Q. Gibson, S. Kushwaha, N. Haldolaarachchige, and R. Cava, Resistivity plateau and extreme magnetoresistance in LaSb, Nat. Phys. **12**, 272 (2016).

[47] S. Sun, Q. Wang, P.-J. Guo, K. Liu, and H. Lei, Large magnetoresistance in LaBi: Origin of field-induced resistivity upturn and plateau in compensated semimetals, New J. Phys. **18**, 082002 (2016).

[48] Y. L. Wang, L. R. Thoutam, Z. L. Xiao, J. Hu, S. Das, Z. Q. Mao, J. Wei, R. Divan, A. Luican-Mayer, G. W. Crabtree, and

W. K. Kwok, Origin of the turn-on temperature behavior in WTe_2, Phys. Rev. B **92**, 180402(R) (2015).

[49] F. F. Tafti, Q. Gibson, S. Kushwaha, J. W. Krizan, N. Haldolaarachchige, and R. J. Cava, Temperature- field phase diagram of extreme magnetoresistance, Proc. Natl. Acad. Sci. USA **113**, E3475 (2016).

[50] X. Du, S.-W. Tsai, D. L. Maslov, and A. F. Hebard, Metal-Insulator-Like Behavior in Semimetallic Bismuth and Graphite, Phys. Rev. Lett. **94**, 166601 (2005).

[51] J. M. Ziman, *Electrons and Phonons: The Theory of Transport Phenomena in Solids* (Oxford University Press, 2001).

[52] R. Singha, A. Pariari, B. Satpati, and P. Mandal, Magnetotransport properties and evidence of a topological insulating state in LaSbTe, Phys. Rev. B **96**, 245138 (2017).

[53] R. Singha, B. Satpati, and P. Mandal, Fermi surface topology and signature of surface Dirac nodes in LaBi, Sci. Rep. **7**, 6321 (2017).

[54] P. M. Hall, S. Legvold, and F. H. Spedding, Electrical resistivity of yttrium single crystals, Phys. Rev. **116**, 1446 (1959).

[55] X. Zhang, Z. Xiao, H. Lei, and Y. Toda, Two-dimensional transition-metal electride Y_2C, Chem. Mater. **26**, 6638 (2014).

[56] M. Kohler, Zur magnetischen widerstandsänderung reiner metalle, Ann. Phys. **424**, 211 (1938).

[57] J. Xu, F. Han, T.-T. Wang, L. R. Thoutam, S. E. Pate, M. Li, X. Zhang, Y.-L. Wang, R. Fotovat, U. Welp, X. Zhou, W.-K. Kwok, D. Y. Chung, M. G. Kanatzidis, and Z.-L. Xiao, Extended Kohler's Rule of Magnetoresistance, Phys. Rev. X **11**, 041029 (2021).

[58] D. V. Khveshchenko, Magnetic-Field-Induced Insulating Behavior in Highly Oriented Pyrolitic Graphite, Phys. Rev. Lett. **87**, 206401 (2001).

[59] See Supplemental Material at http://link.aps.org/supplemental/10.1103/PhysRevB.107.205111 for the following: (i) The 2nd derivative of the raw MR data and the deconvoluted spectrum of F_γ for all temperatures. (ii) The comparison of oscillatory data (extracted from raw MR) originating from the several Fermi sheets. (iii) The calculation of the excitonic gap originating from the applied magnetic field. (iv) Raw Hall data at 50 K and discussion regarding the noise in the Hall measurement. The Supplemental Material also contains Ref. [60].

[60] F. Werner, Hall measurements on low-mobility thin films, J. Appl. Phys. **122**, 135306 (2017).

[61] H. Fritzsche, Electrical properties of germanium semiconductors at low temperatures, Phys. Rev. **99**, 406 (1955).

[62] Y. Kopelevich, V. Lemanov, S. Moehlecke, and J. Torres, Landau level quantization and possible superconducting instabilities in highly oriented pyrolitic graphite, Phys. Solid State **41**, 1959 (1999).

[63] M. Sercheli, Y. Kopelevich, R. Ricardo da Silva, J. Torres, and C. Rettori, Evidence for internal field in graphite: A conduction electron spin-resonance study, Solid State Commun. **121**, 579 (2002).

[64] C. Hurd, *The Hall Effect in Metals and Alloys* (Springer Science & Business Media, 2012).

[65] Y. Saito, The de Haas-van Alphen Effect of InBi, J. Phys. Soc. Jpn. **17**, 716 (1962).

[66] D. Shoenberg, *Magnetic Oscillations in Metals* (Cambridge University Press, 2009).

[67] A. Narayanan, M. D. Watson, S. F. Blake, N. Bruyant, L. Drigo, Y. L. Chen, D. Prabhakaran, B. Yan, C. Felser, T. Kong, P. C. Canfield, and A. I. Coldea, Linear Magnetoresistance Caused by Mobility Fluctuations in *n*-Doped Cd_3As_2, Phys. Rev. Lett. **114**, 117201 (2015).